

Detecting Quasars in Large-Scale Astronomical Surveys

Fabian Gieseke*, Kai Lars Polsterer[†], Andreas Thom*, Peter Zinn[†],
Dominik Bomanns[†], Ralf-Jürgen Dettmar[†], Oliver Kramer[‡], and Jan Vahrenhold*

* Faculty of Computer Science, Technische Universität Dortmund, Dortmund, Germany
{Fabian.Gieseke, Andreas.Thom, Jan.Vahrenhold}@tu-dortmund.de

[†] Department of Physics and Astronomy, Ruhr-University of Bochum, Bochum, Germany
{Polsterer, Zinn, Bomanns, Dettmar}@astro.rub.de

[‡] International Computer Science Institute, Berkeley, USA
okramer@icsi.berkeley.edu

Abstract—We present a classification-based approach to identify quasi-stellar radio sources (quasars) in the Sloan Digital Sky Survey and evaluate its performance on a manually labeled training set. While reasonable results can already be obtained via approaches working only on photometric data, our experiments indicate that simple but problem-specific features extracted from spectroscopic data can significantly improve the classification performance. Since our approach works orthogonal to existing classification schemes used for building the spectroscopic catalogs, our classification results are well suited for a mutual assessment of the approaches’ accuracies.

Index Terms—classification, astronomy, feature extraction

I. INTRODUCTION

The automated analysis of data sets has become an increasingly important issue for researchers in astronomy [2], [4]. This is in particular the case for massive data sets obtained from, e.g., the *Sloan Digital Sky Survey* (SDSS), which is said to be “one of the most ambitious and influential surveys in the history of astronomy” [12]. The latter catalog is currently based on raw data of about 60 terabytes and the trend towards data-intensive science seems to become even more evident with near-future projects such as the *Large Synoptic Sky Telescope* [9], which will produce data volumes in the petabyte range. From a machine learning perspective, a variety of problems in astronomy can be formulated as supervised (e.g. classification, regression) or unsupervised tasks (e.g. clustering, dimensionality reduction), and the corresponding tools for addressing these tasks have been recognized as “increasingly essential in the era of data-intensive astronomy” [4].

We describe the use of supervised learning techniques to discriminate quasars from other celestial objects. We approach this problem from a machine learning point of view and analyze how the generalization performance of standard classifiers can be improved by incorporating simple problem-specific features which are motivated by the physical properties of quasars and other celestial objects. Although some classification problems have already been addressed in the field of astronomy, the interface between both communities is not well defined [4]. One of the goals of this paper is to work towards bridging the gap between both communities by

describing an important astronomical classification problem (along with some physical background) and by preparing the corresponding data such it can be approached easily from a machine learning point of view.

II. BACKGROUND

One of the main objectives of the SDSS consisted in finding *quasi-stellar radio sources (quasars)*, a special kind of *Active Galactic Nuclei* (AGN). Due to their extreme luminosities, quasars are among the most distant objects in the universe that can be observed. Depending on this distance it takes up to billions of years for the emitted radiation to reach the Earth. Therefore this radiation reveals information about the long ago state of a quasar and thus about the early universe.

The widely accepted explanation for the nature of these extreme sources that reach the highest luminosities among all known astrophysical phenomena is the so-called *unified model* [15]. This model reduces the large number of different types of AGN to a single phenomenon: a *Supermassive Black Hole* (SMBH) surrounded by a thick dust torus that is accreting material. It is heated to extremely high temperatures [3] and thus produces radiation in nearly all frequency bands. The differences in how we observe AGNs is mainly caused by the inclination of the surrounding dust torus. If the inclination angle is small, we are able to observe the inner parts of the torus. In this case either an optically bright quasar or even a highly variable blazar is detected. The broad emission lines in the spectrum of a quasar (see below) result from the fact that, while observing the direct vicinity of the SMBH, one observes a region with a higher gravitational potential and thus higher orbiting velocities of the accretion disk material. Such high velocities yield to a Doppler-broadening of the emission lines, in this strength only present for AGN-powered sources.

a) *Related Work*: The problem of identifying quasars has already been addressed in the field of astronomy with a focus on photometric data, see, e.g., the overview given by Ball and Brunner [2] and the references therein. To the best of our knowledge, the work reported upon in this paper is the first extensive machine-learning-based study on classifying quasars given spectroscopic data.

III. DATA

Our classification approaches work on a subset of the SDSS (DR6) [12] database. This data has been obtained via a 2.5-meter telescope at the Apache Point Observatory (New Mexico) which is equipped with two special-purpose instruments: a 120-megapixel camera and a pair of spectrographs. Both types of resulting data, namely the photometric as well as the spectroscopic data, are used in this work.

A. Labels

To obtain ground truth data, we asked an expert to manually label (based on normalized plots) a random subset of 5,261 spectra out of the 1,271,680 spectra available in the SDSS. The resulting catalog contains IDs and labels of 512 objects of type “quasar” and 4,749 objects of type “other”.¹

B. Photometric Data

The 120-megapixel camera collects simultaneously data through five different filters. By doing drift-scanning, those data sets are combined to overlaying stripes that cover five wavelength ranges per observation. These wavelength ranges are the so-called *u*, *g*, *r*, *i*, and *z* bands. In each of these bands, the SDSS photometric pipeline automatically extracts data for all celestial objects. Finally, in addition to the segmented raw data stripes, a batch of extracted photometric features is available for each object in each band.

One group of these photometric features, the so-called *magnitudes*, are logarithmic measures of the brightness of an object. Among the most established approaches for data fitting are the *PSF*, the *Petrosian*, and the *Model* approach [12]. The output of these approaches can be retrieved from the `PhotoObjAll` table of the *Catalog Archive Server* (CAS) [12] and, since extracted from five bands, yields the following set of photometric features:

- 1) PSF magnitudes: `psfMag_u`, `psfMag_g`, `psfMag_r`, `psfMag_i`, `psfMag_z`
- 2) Petrosian magnitudes: `petroMag_u`, `petroMag_g`, `petroMag_r`, `petroMag_i`, `petroMag_z`
- 3) Model magnitudes: `modelMag_u`, `modelMag_g`, `modelMag_r`, `modelMag_i`, `modelMag_z`

C. Spectroscopic Data

The raw spectra of all manually labeled objects have been retrieved from the *Data Archive Server* (DAS) [12]. Each spectrum contains the flux values for roughly 3,850 wavelengths. In order to obtain raw features that are independent of the specific wavelengths, the spectra of all considered objects have been aligned and truncated. This results in a set of spectra having $d = 3,825$ features, see Figure 1.

D. Quality of the Data Sample

To estimate the quality of our data sample, we consider an important astronomical property, namely the *redshift* (*value*) of an object [12]. In Figure 2, the distribution (based on the

¹The induced catalog along with the photometric and spectroscopic data can be obtained from the authors upon request.

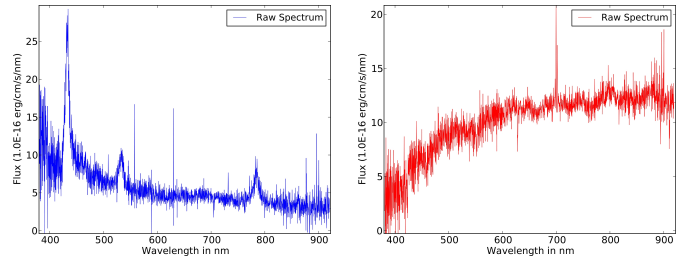


Fig. 1. Spectroscopic data for the manually labeled training set, which consists of objects of type “quasars” (blue) and of type “other” (red).

z -values in the SDSS database) of all 512 quasars present in our data set is given. It can be seen that these objects cover a redshift range of up to $z = 5$ and that the majority has a low redshift ($z < 2.3$). The remaining objects are dominated by 4,053 galaxies exhibiting a low redshift.

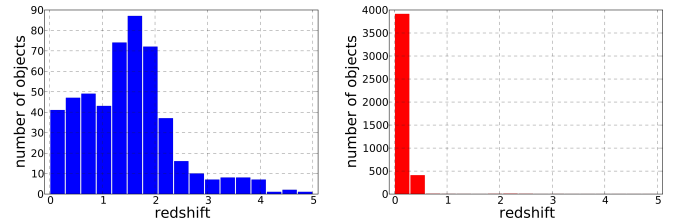


Fig. 2. Redshift distribution of quasars (left) and other objects (right).

In Figure 3, the labels available in the SDSS database are compared with our manually obtained labels. Here, the blue plot corresponds to all 512 objects classified as objects of type “quasar” by our expert; the red plot corresponds to the remaining objects of type “other”. The x -axis of both plots is based on the labels present in the SDSS database. It can be clearly seen that the labeling of our expert is in agreement with the one of the SDSS-pipeline.²

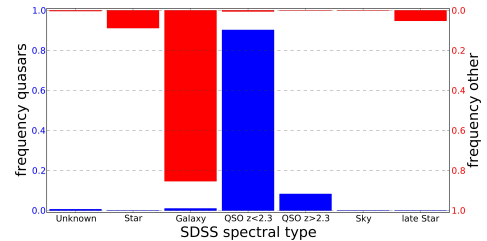


Fig. 3. Comparison of our expert’s manual labeling with the corresponding labeling of the SDSS database.

IV. CLASSIFICATION APPROACHES

The labeled data induces a (training) set $T = \{(\mathbf{x}_1, y_1), \dots, (\mathbf{x}_n, y_n)\} \subset \mathbb{R}^d \times \{-1, +1\}$ containing the

²It should be pointed out that the SDSS-pipeline is also based on human verification of the labels and, hence, can only be seen as a semi-automatic classification approach.

features and labels for each object, where the positive class corresponds to all objects of type "quasar". We apply two well-known classification approaches, namely *k-Nearest Neighbors (kNNs)* and *Support Vector Machines (SVMs)*. For completeness, we depict the key ideas of both classification models and refer to the corresponding literature for details [13], [14], [16].

A. *k-Nearest Neighbors*

The *k-Nearest Neighbor* classifier uses the *k* "closest" objects from the given set of already classified objects to assign a class to an unclassified object [14]. More precisely, the (binary) classification $\hat{Y}(\mathbf{x})$ for an object \mathbf{x} is

$$\hat{Y}(\mathbf{x}) = \begin{cases} 1 & \text{if } f(\mathbf{x}) > 0 \\ -1 & \text{if } f(\mathbf{x}) \leq 0, \end{cases} \quad (1)$$

where

$$f(\mathbf{x}) = \sum_{\mathbf{x}_i \in N_k(\mathbf{x})} y_i, \quad (2)$$

and where $N_k(\mathbf{x})$ denotes the *k*-nearest neighbors in the training set with respect to \mathbf{x} . To define "closeness", arbitrary metrics can be used; a popular choice is the Euclidean metric (which we use for the experimental evaluation as well).

B. *Support Vector Machines*

The aim of a SVM consists in finding a hyperplane in a feature space which maximizes the "margin" between both classes such that only few training patterns lie within the margin [13], [16]. The latter task can be formulated as an optimization problem, where the first term corresponds to maximizing the margin and the second term to the loss caused by patterns lying within the margin:

$$\begin{aligned} & \underset{\mathbf{w} \in \mathcal{H}_0, \xi \in \mathbb{R}^n, b \in \mathbb{R}}{\text{minimize}} && \frac{1}{2} \|\mathbf{w}\|^2 + C \sum_{i=1}^n \xi_i \\ & \text{s.t. } && y_i(\langle \mathbf{w}, \Phi(\mathbf{x}_i) \rangle + b) \geq 1 - \xi_i, \\ & && \text{and } \xi_i \geq 0, \end{aligned} \quad (3)$$

where $C > 0$ is a user-defined parameter. The function $\Phi : \mathbb{R}^d \rightarrow \mathcal{H}_0$ mapping the patterns into a feature space \mathcal{H}_0 is induced by a kernel function $k : \mathbb{R}^d \times \mathbb{R}^d \rightarrow \mathbb{R}$ with $k(\mathbf{x}_i, \mathbf{x}_j) = \langle \Phi(\mathbf{x}_i), \Phi(\mathbf{x}_j) \rangle$. A kernel function can be seen as a "similarity measure" for input patterns. The goal of the learning process is to find the optimal hyperplane $f(\mathbf{x}) = \langle \mathbf{w}, \Phi(\mathbf{x}) \rangle + b$. Unseen objects can subsequently be classified via Equation (1). A common choice for the kernel function is the linear kernel

$$k(\mathbf{x}_i, \mathbf{x}_j) = \langle \mathbf{x}_i, \mathbf{x}_j \rangle \quad (4)$$

or the RBF kernel

$$k(\mathbf{x}_i, \mathbf{x}_j) = \exp\left(-\frac{\|\mathbf{x}_i - \mathbf{x}_j\|^2}{2\sigma^2}\right), \quad (5)$$

where the parameter σ is called the *kernel width*.

V. SPECTROSCOPIC FEATURE EXTRACTION

As discussed in Section II, the physical properties of quasars result in characteristic, broad emission lines. Our approach consists in extracting meaningful features given "continuum-subtracted" versions of the raw spectra. In the remainder of this section, we provide two ways for estimating the continuum (i.e. the rough shape) of a spectrum. Given such an estimate, we define several features motivated by the physical properties of quasars and non-quasars.

A. *Continuum Extraction with Splines*

The first approach for extracting the continuum is based on splines [6]. In a first step, we use a sliding-window technique to merge consecutive features (flux values) and to obtain a "binned" version of the spectroscopic data. This binned spectrum is subsequently normalized and smoothed using the Savitzky-Golay-Filter [11] (which is a standard smoothing filter), see the black curve shown in Figure 4. Since the broad emission lines present in a quasar's spectroscopic data lead to an overestimation of the continuum, we apply an additional smoothing method to reduce the influence of the peak intensities. Given such a smoothed spectrum, we perform a spline interpolation to extract the estimated continuum (red curve). Finally, the difference of the smoothed spectrum and the estimated continuum is evaluated by rounding "nonrelevant" values within a δ -range around the continuum, where δ is computed as the standard deviation of all calculated differences. The resulting "continuum-subtracted" spectrum is represented by the green curve in Figure 4.

B. *Continuum Extraction with Support Vector Regression*

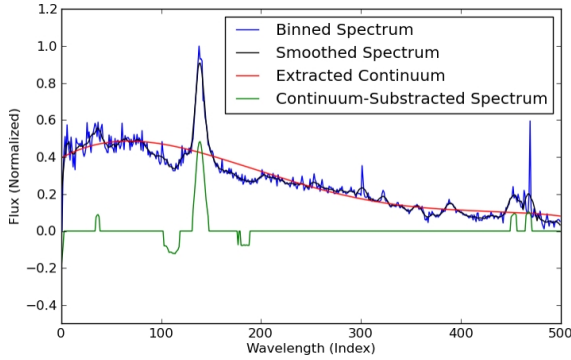
Our second approach for estimating the continuum is based on the concept of *support vector regression (SVR)* [13] which can be considered to be a special case of regularization problems of the form

$$\inf_{f \in \mathcal{H}} \frac{1}{n} \sum_{i=1}^n L(y_i, f(\mathbf{x}_i)) + \lambda \|f\|_{\mathcal{H}}^2, \quad (6)$$

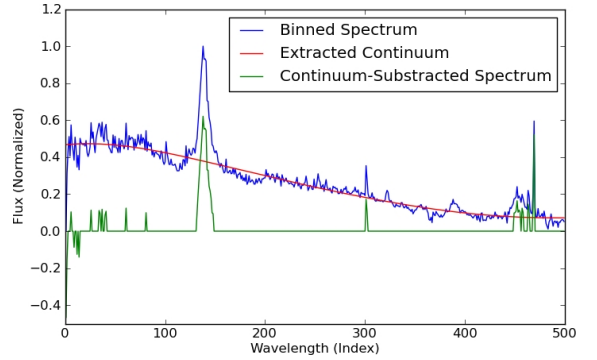
where $\lambda > 0$ is a fixed real number, $L : \mathbb{R} \times \mathbb{R} \rightarrow [0, \infty)$ is a *loss function* and $\|f\|_{\mathcal{H}}^2$ is the squared norm in a *reproducing kernel Hilbert space (RKHS)* $\mathcal{H} \subseteq \mathbb{R}^X = \{f : X \rightarrow \mathbb{R}\}$ induced by the associated kernel function (note that, in this case, the kernel function is defined on the indices associated with the flux vales). By plugging in the so-called ε -intensive loss with $\varepsilon > 0$ one obtains

$$\inf_{f \in \mathcal{H}} \frac{1}{n} \sum_{i=1}^n \max(|f(\mathbf{x}_i) - y_i| - \varepsilon, 0) + \lambda \|f\|_{\mathcal{H}}^2, \quad (7)$$

which depicts the optimization problem of SVR. Here, the first term corresponds to the "difference" between the (continuum) model and the data and the second term corresponds to the "complexity" of the (continuum) model. Ideally, one would like to have a model which fits the data well and which is not too "complex". Additionally (and in contrast to standard regression problems), we would like to "ignore" the broad



(a) Spline Model



(b) Support Vector Regression Model

Fig. 4. Estimation of the continuum with splines and support vector regression.

emission lines present in the quasars’ spectra, see Figure 4. Two properties of the SVR approach are advantageous in this context: First, the ϵ -intensive loss function penalizes the differences of the model and the flux values only linearly (in contrast to, e.g., the square-loss [13]). Second, by adapting the involved parameters, one can adjust the behavior of the model such that the influence of large peaks is reduced.³

Given the resulting continuum models, we compute the continuum subtracted spectra by considering the difference between each continuum model and the corresponding input spectrum while ignoring values lying within a small δ -range around the continuum model (like above).

C. Extracted Features

Given the estimated continuum and thus the continuum-subtracted spectra, we try to extract meaningful features representing the main characteristics of typical quasars, see Table I: Since the (true) continuum of a quasar’s spectrum is normally horizontal or decreasing, we use the first and the last value of the computed continuum as features to estimate the rough slope of the spectrum (F1 and F2). As described in Section II, broad emission lines provide an excellent characteristic for experts to classify quasars. The remaining eight features aim at capturing these “peak properties”. Here, features F3 and F4 denote the absolute values of the sum of all “positive” and “negative” peaks, respectively. Further, features F5, F6, F9, and F10 indicate the width and the face of the strongest peaks. Finally, features F7 and F8 capture the minimum and maximum peak intensities.

VI. EXPERIMENTS

We consider several data sets which are based on the photometric and spectroscopic data in order to evaluate the generalization performances of our approaches. In the remainder of this section, we provide a description of these data sets as well as a description of the experimental setup and the final outcome of the experimental evaluation.

³For instance, the kernel width σ of the (used) RBF kernel can be adjusted such that large peaks have less influence on the continuum model.

TABLE I
EXTRACTED FEATURES

Feature	Description
F1	First value of the extracted continuum
F2	Last value of the extracted continuum
F3	Integral of all positive peaks
F4	Integral of all negative peaks
F5	Width of the broadest positive peak
F6	Width of the broadest negative peak
F7	Major peak intensity
F8	Minor peak intensity
F9	Major face of positive peak
F10	Major face of negative peak

A. Data Sets

Given the data, we generate a variety of data sets, see Table II. Each data set contains all $N = 5,261$ objects and, thus, all $p = 512$ objects of type “quasar” and all $n = 4,749$ objects of type “other”. The first four data sets D1–D4 are based on the different magnitudes which are retrieved from the photometric data, see Section III. The data sets D5–D7 are binned versions of the raw spectra, i.e., the original input dimension (3,825) of each spectrum is reduced to $d = 5$, $d = 100$ and $d = 500$ respectively by “averaging” consecutive flux values such that the desired output dimension is obtained. The data sets D8 and D9 are obtained via the spectroscopic feature extraction approaches depicted in Section V, where we use binned versions of the spectra with $d = 500$ dimensions as starting point. The last data set D10 is based on the spectroscopic feature extraction (SVR) in combination with a set of photometric features.⁴

B. Experimental Setup

Except for the SVM implementation, all preprocessing steps and algorithms are implemented in Python. For the SVM model, we resort to the LIBSVM implementation provided by Chang and Lin [5].

⁴This data set aims at the situation, where both parts of the data (photometric and spectroscopic) are given for all objects (which is the case for, e.g., the LAMOST project [8]).

TABLE II
CONSIDERED DATA SETS

Data Set	Features
D1	psfMag_u - psfMag_g, psfMag_g - psfMag_r, psfMag_r - psfMag_i, psfMag_i - psfMag_z
D2	psfMag_u, psfMag_g, psfMag_r, psfMag_i, psfMag_z
D3	psfMag_u, psfMag_g, psfMag_r, psfMag_i, psfMag_z, modelMag_u, modelMag_g, modelMag_r, modelMag_i, modelMag_z
D4	psfMag_u, psfMag_g, psfMag_r, psfMag_i, psfMag_z, petroMag_u, petroMag_g, petroMag_r, petroMag_i, petroMag_z
D5	BinnedSpec5
D6	BinnedSpec100
D7	BinnedSpec500
D8	ExtractedFeatures (SPLINE)
D9	ExtractedFeatures (SVR)
D10	ExtractedFeatures (SVR), psfMag_u, psfMag_g, psfMag_r, psfMag_i, psfMag_z, modelMag_u, modelMag_g, modelMag_r, modelMag_i, modelMag_z

b) *Parameters*: To train and evaluate the classification approaches, half of each data set is used as training and the other half as test set. For the SVM model, a RBF kernel with kernel width σ is used. The corresponding model parameters k , C , and σ for both classification approaches are tuned via 10-fold cross-validation [14] on the training set given a grid of parameters ($k \in \{1, \dots, 10\}$ for kNN and $(C, \sigma) \in \{2^{-10}, 2^{-9}, \dots, 2^{+10}\} \times \{2^{-10}, 2^{-9}, \dots, 2^{+10}\}$ for the SVM). For the spectroscopic feature extraction, we set the involved parameters to fixed values for all spectra: For the spline-based approach, the binned spectrum is smoothed using the Savitzky-Golay-filter of degree 3 and window size 15. Afterwards we use the interpolation package of the `Scipy` library [7] for estimating the smoothed spline of order 4 and smoothing factor 100. For the SVR-based approach, we again make use of the `LIBSVM` implementation using a RBF kernel and input parameters $C = 100$, $\gamma = 0.00001$, and $\epsilon = 0.1$.

c) *Measuring the Classification Performance*: The performances of our models are evaluated on the test set. Since our data sets are imbalanced, we resort to the *Matthews Correlation Coefficient* (MCC) [10] as quality measure:

$$\frac{TP \cdot TN - FP \cdot FN}{\sqrt{(TP + FN)(TP + FP)(TN + FP)(TN + FN)}}$$

Here, TP , FP , TN and FN denote the number of true positives, false positives, true negatives, and false negatives, respectively [1], [10]. We also provide the *true positive rate* (TP -rate) given by TP/p as well as the *false positive rate* (FP -rate) given by FP/n , which can be seen as “hit rate” and “false alarm rate”, respectively [1]. Finally, we consider the *error* on the test set given by $(FP + FN)/N$ which simply measures the overall number of misclassifications.

C. Results

In the remainder of this section, we discuss the outcome of the conducted experiments.

TABLE III
CLASSIFICATION PERFORMANCES

Data Set	kNN			
	MCC	Error	TP - rate	FP - rate
D1	0.873	2.32%	86.1%	1.0%
D2	0.826	3.15%	81.7%	1.4%
D3	0.902	1.82%	91.2%	1.0%
D4	0.893	2.01%	91.6%	1.3%
D5	0.748	4.41%	70.6%	1.5%
D6	0.824	3.15%	80.2%	1.2%
D7	0.808	3.42%	77.7%	1.2%
D8	0.963	0.69%	95.6%	0.3%
D9	0.959	0.76%	96.7%	0.5%
D10	0.971	0.53%	96.3%	0.2%

Data Set	SVM (RBF)			
	MCC	Error	TP - rate	FP - rate
D1	0.859	2.54%	84.2%	1.0%
D2	0.851	2.74%	85.0%	1.3%
D3	0.922	1.44%	91.9%	0.7%
D4	0.908	1.71%	91.5%	0.9%
D5	0.757	4.33%	73.6%	1.8%
D6	0.788	3.69%	71.7%	0.8%
D7	0.610	6.23%	44.0%	0.5%
D8	0.965	0.65%	96.0%	0.3%
D9	0.977	0.42%	97.4%	0.2%
D10	0.971	0.53%	96.7%	0.2%

d) *Classification Performance*: The classification performances of both classification approaches on the various data sets are shown in Table III, where the best results are highlighted (bold face type). Both the kNN and the SVM model perform well on the first four data sets, which are composed of the magnitudes retrieved from the photometric data.⁵ While the performance is worse on the data sets containing the binned versions of the spectra (D5–D7), it improves significantly when the extracted features (D8 and D9) are used as input data. Using additional photometric features (D10) does not lead to an improvement.

e) *How Much Spectroscopic Data is Needed*: The spectroscopic feature extraction approaches used for the data sets D8–D10 are based on binned versions of the raw spectra containing $d = 500$ values. A natural question is “how detailed” these binned versions have to be such that the spectroscopic feature extraction yields good results. One of the benefits of being able to use “low detailed” versions of the raw spectra is the performance gain with respect to the computation time (which will be of tremendous importance for an efficient classification of larger portions of the SDSS or even the full catalog).

In Figure 5, the influence of the input dimension on the classification performance (MCC) is shown. The plot indicates a quite similar classification performance of both approaches on all considered data sets. Further, it seems that data sets based on input dimensions of roughly $d = 200$ already yield

⁵We would like to point out that a generalization of these results to the complete photometric catalog is dubious due to the fact that the sample is biased (a target selection criteria was used for collecting the spectroscopic data [12]).

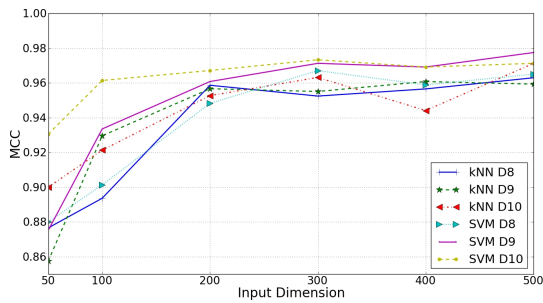


Fig. 5. Influence of the input dimension on the MCC.

good results, which cannot be improved significantly by using a higher input precision. We expect this observation to be helpful when considering a time/classification quality trade-off for processing massive databases, e.g. in the context of the LAMOST project [8].

VII. CONCLUSIONS AND OUTLOOK

We have considered the task of using classification algorithms to discriminate quasars from other objects given photometric and spectroscopic data. In recent years, problems of this kind have gained more and more attention in the field of astronomy due to the fact that the massive amounts of data arising nowadays cannot be handled without automatic (machine learning) approaches. While the problem of detecting quasars (especially using only photometric data) has already been considered in the field of astronomy, we are not aware of corresponding literature (with respect to spectroscopic data) in the field of machine learning, and the orthogonality of the existing and proposed approaches seems to allow for a mutually beneficial collaboration between these fields. The sheer volume of astronomical data that is already available or will be available in the near future emphasizes the need for high-performance machine learning algorithms.

REFERENCES

- [1] Ethem Alpaydin. *Introduction to Machine Learning*. MIT Press, second edition, 2010.
- [2] Nicholas M. Ball and Robert J. Brunner. Data mining and machine learning in astronomy. arXiv:0906.2173v1 [astro-ph.IM], June 2009.
- [3] E. W. Bonning, L. Cheng, G. A. Shields, S. Salviander, and K. Gebhardt. Accretion Disk Temperatures and Continuum Colors in QSOs. *The Astrophysical Journal*, 659:211–217, April 2007.
- [4] Kirk Borne. Scientific data mining in astronomy. arXiv:0911.0505v1 [astro-ph.IM], November 2009.
- [5] Chih-Chung Chang and Chih-Jen Lin. *LIBSVM: a library for support vector machines*, 2001. Software available at <http://www.csie.ntu.edu.tw/~cjlin/libsvm>.
- [6] Bernard Francis Hildebrand. *Introduction to numerical analysis: 2nd edition*. Dover Publications, Inc., New York, NY, USA, 1987.
- [7] Eric Jones, Travis Oliphant, Pearu Peterson, et al. *SciPy: Open source scientific tools for Python*, 2001. Software available at <http://www.scipy.org/>.
- [8] Large Sky Area Multi-Object Fiber Spectroscopic Telescope (LAMOST). <http://www.lamost.org/>, 2010.
- [9] Large Synoptic Survey Telescope (LSST). <http://www.lsst.org>, 2010.
- [10] B. W. Matthews. Comparison of the predicted and observed secondary structure of t4 phage lysozyme. *Biochimica et Biophysica Acta*, 405(2):442–451, 1975.
- [11] A. Savitzky and M.J.E. Golay. Smoothing and Differentiation of Data by Simplified Least Squares Procedures. *Analytical Chemistry*, 36:1627–1639, 1964.
- [12] Sloan Digital Sky Survey (SDSS). <http://www.sdss.org>, 2010.
- [13] Ingo Steinwart and Andreas Christmann. *Support Vector Machines*. Springer-Verlag, New York, USA, 2008.
- [14] Robert Tibshirani and Jerome Friedman Trevor Hastie. *The Elements of Statistical Learning*. Springer, 2009.
- [15] C. M. Urry and P. Padovani. Unified Schemes for Radio-Loud Active Galactic Nuclei. *Publications of the Astronomical Society of the Pacific*, 107:803–845, September 1995.
- [16] Vladimir Vapnik. *Statistical Learning Theory*. Wiley, New York, 1998.